Hadis Morkoç and Ümit Özgür

Zinc Oxide

Fundamentals, Materials and Device Technology

Hadis Morkoç and Ümit Özgür
Zinc Oxide

Related Titles

Neumark, G. F., Kuskovsky, I. L., Jiang, H. (eds.)

Wide Bandgap Light Emitting Materials And Devices

2007
ISBN: 978-3-527-40331-8

Capper, P., Mauk, M. (eds.)

Liquid Phase Epitaxy of Electronic, Optical and Optoelectronic Materials

2007
ISBN: 978-0-470-85290-3

Hadis Morkoç and Ümit Özgür

Zinc Oxide

Fundamentals, Materials and Device Technology

The Authors

Prof. Dr. Hadis Morkoç
Virginia Commonwealth University
Dept. of Electrical Engineering
Richmond, VA
USA

Ümit Özgür
Virginia Commonwealth University
Dept. of Electrical Engineering
Richmond, VA
USA

Contents

Preface

The semiconductor ZnO has gained substantial interest in the research community in part because of its large exciton binding energy (60 meV) that could lead to lasing action based on exciton recombination and possibly polariton/exciton interaction even above room temperature. The motivation for this book stems from the applications of ZnO in potential optical devices, transparent ohmic contacts, light extraction enhancement structures for GaN-based light-emitting diodes (LEDs), transparent thin-film transistors, transducers, and so on, for which ZnO is well suited.

We should mention that even though research focusing on ZnO goes back to many decades, the renewed interest is fuelled by the availability of high-quality substrates and reports of p-type conduction and ferromagnetic behavior when doped with transition metals, both of which remain controversial. The lattice parameter studies date back to 1935 [1], vibrational properties were studied by Raman scattering in 1966 [2], detailed optical properties were investigated in 1954 [3], and its growth by chemical vapor transport was attained in 1970 [4]. In terms of devices, Au Schottky barriers were formed in 1965 [5], LEDs were demonstrated in 1967 [6] wherein Cu2O was used as the p-type material, metal insulator semiconductor (MIS) structures were reported in 1974 [7], ZnO/ZnTe n–p junctions were accomplished in 1975 [8], and Al/Au ohmic contacts were reported in 1978 [9]. Very high quality what used to be called whiskers and platelets, the nomenclature that gave way to nanostructure, of late, have been prepared early on and used to deduce much of the principal properties of this material, particularly the optical properties, albeit with a healthy debate about the valence band ordering and assignment of some of the peaks appearing in optical excitation measurements. In addition to the requisite direct bandgap, the attraction to ZnO can simply be attributed to its large exciton binding energy of 60 meV, which might potentially pave the way for efficient room-temperature exciton-based and/or polariton/exciton interaction-based lasers with very low-threshold currents. The field is also fuelled by theoretical predictions and perhaps experimental confirmation of ferromagnetism at room temperature for potential spintronics applications. Of paramount importance is the transparency of ZnO to visible light that is in part responsible for exploring this material for applications such as transparent ohmic contacts for light emitters based on GaN, solar cells that have been gaining considerable interest, transparent thin-film transistors, and nanostructures that can be used to extract light from LEDs such as those

based on GaN. Furthermore, highly piezoelectric nature of ZnO and its favorable electromechanical coupling coefficient are very attractive for devices such as surface acoustic waves.

This book is unique in the sense that it represents the first cohesive treatment of the entire field of ZnO and related materials and devices under one cover. As such, much needed continuity and smooth flow are provided without duplications. The aspects of ZnO forming the basis for this book are presented in eight chapters, the contents of which are elaborated on below.

Chapter 1 treats the mechanical–thermal, chemical, and electrical properties of ZnO. Low-field as well as high-field transport is discussed. Chapter 2 discusses the growth of ZnO and heterostructures by popular techniques such as sputtering, molecular beam epitaxy, pulsed laser deposition, and chemical vapor deposition. Substrates on which ZnO is deposited along with resultant properties of the material are also discussed. Chapter 3 provides the most comprehensive treatment of optical properties of ZnO that are rich not only in terms of linear processes but also in terms of nonlinear processes. In this vein, following an introduction to optical processes in semiconductors, the specifics of optical transitions related to free excitons and polaritons, bound excitons, two-electron satellite transitions are treated in detail. This segues into the discussion of defect-related transitions such as the celebrated green, yellow, and red transitions. After discussing the refractive index of ZnO and its ternary ZnMgO, a detailed discussion of stimulated emission in ZnO is given, including single-crystal and polycrystal forms and quantum wells. The treatment then moves on to the discussion of recombination dynamics looking at the recombination lifetimes. The attention is then turned onto nonlinear optical properties including second- and third-order harmonic generation, intensity-dependent refractive index, and two-photon absorption.

Chapter 4 discusses the all-important doping in ZnO, in particular p-type doping. Details and motivations for approaches taken for attaining p-type conductivity inclusive of codoping methods and characterization schemes are provided. Chapter 5 deals with doping ZnO with magnetic ions in the context of dilute magnetic semiconductors. A sufficient amount of the theory of magnetization, classification of magnetic materials, measurement techniques, and theoretical and experimental investigations of magnetic ion-doped ZnO such as Mn and Co, among others, are discussed.

Chapter 6 discusses bandgap engineering that forms the basis for many of the high-performance electrical and optical devices based on semiconductors. ZnO alloyed with Mg and Be for increasing its bandgap and alloyed with Cd for decreasing its bandgap is discussed with the accompanying issues with regard to changes in the lattice constant and of course the bandgap. Chapter 7 paves the way for nanostructures based on ZnO. After the discussion of most popular nanostructure fabrication techniques, the application of these techniques to ZnO nanostructures such as nanorods (nanowires), nanobelts, and polypod systems is discussed.

The book ends with the discussion of ZnO processing needed for devices, metal semiconductors contacts and their current–voltage relationships including the fundamentals of current conduction mechanisms in various regimes, etching of

ZnO, and heterostructure devices. Among the devices, light emitters, microcavities, optically pumped lasers, photodiodes, metal–insulator–semiconductor diodes, field-effect transistors, transparent conducting oxides, and transparent thin-film transistors based on ZnO, piezoelectric devices in the form of surface acoustic wave devices, and gas and biosensor followed by solar cells cap the discussion.

It is not only fair but gratifying to state that we owe so much to so many including our family members, friends, coworkers, colleagues, and those who contributed to the field of semiconductors in general and ZnO in particular in our efforts to bring this manuscript to the service of readers. To this end, HM would like to thank his wife Amy and son Erol for at least their understanding why he was not really there for them fully during the preparation of this manuscript, which took longer than most could ever realize. UO wants to thank his parents and his sister for their continuing support throughout his career. Also, without the support of VCU, our past Dean R.J. Mattauch and current Dean R.D. Jamison, past assistant Dean Susan Younce, Department Chair A. Iyer, and our coworkers and students, it would not have been possible to pursue this endeavor.

Special recognitions also go to our coworkers Dr Y.I. Alivov, Dr V. Avrutin, Dr N. Izyumskaya, and Professor M. Reshchikov for their contributions to the research that made possible the discussions on growth, devices, and point defects a much more manageable task.

Special thanks go to J.M. Recio, S. Desgreiners, J. Pollmann, J.E. Jaffe, F. Decremps, M. Schubert, C. Bundesmann, N. Ashkenov, T. Sekiguchi, T. Fukuda, J.-J. Song, J. Nause, P. Ruterana, Q. Wang, Y. Chen, T. Yao, K. Thonke, C. G. van de Walle, P. Dahan, B. Meyer, S.-J. Park, A. Krost, X. Feng, T. Fukumura, Y.-H. Jeong, G. Lawes, I. Tanaka, D.P. Norton, N.H. Hong, J.M.D. Coey, M.H. Kane, T.-S. Chin, Y. Ishida, K. Ando, A. Ohtomo, T. Makino, P. Yang, Z.L. Wang, A.B. Djurišić, G.-C. Yi, B.P. Zhang, M. Kawasaki, R. Shimada, D. Hofstetter, Y. Lu, S. Fujita, N.H. Nickel, B. Gil, R.L. Hoffman, J. Fallert, and C.K. Klingshirn for willingly devoting considerable time and effort to provide us with digital copies of figures and high-quality images. They are also acknowledged in conjunction with the figures.

Richmond, VA, June 2008   *Hadis Morkoç and Ümit Özgür*

References

1 Bunn, C.W. (1935) *Proceedings of the Physical Society*, **47**, 835.

2 Damen, T.C., Porto, S.P.S. and Tell, B. (1966) *Physical Review*, **142**, 570.

3 Mollwo, E. (1954) *Zeitschrift fur Angewandte Physik*, **6**, 257.

4 Galli, G. and Coker, J.E. (1970) *Applied Physics Letters*, **16**, 439.

5 Mead, C.A. (1965) *Physics Letters*, **18**, 218.

6 Drapak, I.T. (1968) *Semiconductors*, **2**, 624.

7 Minami, T., Tanigava, M., Yamanishi, M. and Kawamura, T. (1974) *Japanese Journal of Applied Physics*, **13**, 1475.

8 Tsurkan, A.E., Fedotova, N.D., Kicherman, L.V. and Pas'ko, P.G. (1975) *Semiconductors*, **6**, 1183.

9 Brillson, L.J. (1978) *Journal of Vacuum Science & Technology*, **15**, 1378.

1
General Properties of ZnO

In this chapter, crystal structure of ZnO encompassing lattice parameters, electronic band structure, mechanical properties, including elastic constants and piezoelectric constants, lattice dynamics, and vibrational processes, thermal properties, electrical properties, and low-field and high-field carrier transport is treated.

1.1
Crystal Structure

Most of the group II–VI binary compound semiconductors crystallize in either cubic zinc blende or hexagonal wurtzite (Wz) structure where each anion is surrounded by four cations at the corners of a tetrahedron, and vice versa. This tetrahedral coordination is typical of sp^3 covalent bonding nature, but these materials also have a substantial ionic character that tends to increase the bandgap beyond the one expected from the covalent bonding. ZnO is a II–VI compound semiconductor whose ionicity resides at the borderline between the covalent and ionic semiconductors. The crystal structures shared by ZnO are *wurtzite* (B4), *zinc blende*[1] (B3), and *rocksalt* (or Rochelle salt)[2] (B1) as schematically shown in Figure 1.1. B1, B3, and B4 denote the *Strukturbericht*[3] designations for the three phases. Under ambient conditions, the thermodynamically stable phase is that of wurtzite symmetry. The zinc blende ZnO structure can be stabilized only by growth on cubic substrates, and

---

[1] The term zinc blende originated from compounds such as ZnS, which could be in cubic or hexagonal phase. But the term has been used ubiquitously for compound semiconductors with cubic symmetry. The correct term that should be used for the cubic phase of ZnO GaN is actually *sphalerite*. To be consistent with the diction throughout the literature even at the expense of bordering inaccuracy, the term zinc blende is used throughout this book.

[2] Also called Seignette salt – named after Pier Seignette from La Rochelle, France, who first prepared potassium sodium tartrate tetrahydrate (KNaC$_4$H$_4$O$_6$·4H$_2$O) in 1675 and determined its structure.

[3] *Strukturbericht*, the original crystallographic reports. From 1919 to 1939 (Vols 1–8), they were published in Germany. Since then, they have been published in the United States under the name *Structure Reports, Acta Crystallographica Section E*, by the International Union of Crystallography.
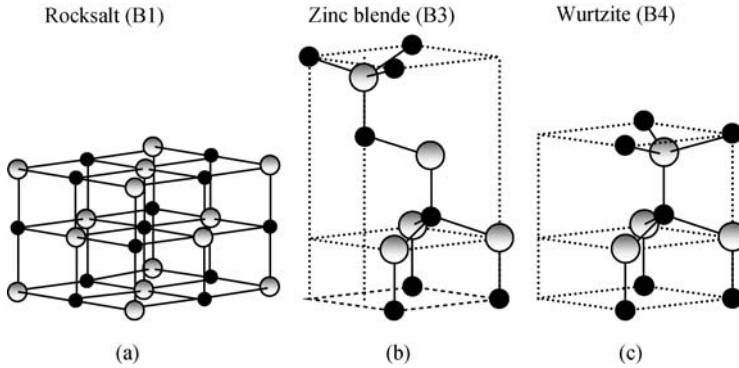
Figure 1.1 Stick-and-ball representation of ZnO crystal structures: (a) cubic rocksalt (B1), (b) cubic zinc blende (B3), and (c) hexagonal wurtzite (B4). Shaded gray and black spheres denote Zn and O atoms, respectively.

the rocksalt or Rochelle salt (NaCl) structure may be obtained at relatively high pressures, as in the case of GaN.

The *wurtzite* structure has a hexagonal unit cell with two lattice parameters a and c in the ratio of $c/a = \sqrt{8/3} = 1.633$ (in an ideal wurtzite structure) and belongs to the space group C_{6v}^4 in the Schoenflies notation and $P6_3mc$ in the Hermann–Mauguin notation. A schematic representation of the wurtzitic ZnO structure is shown in Figure 1.2. The structure is composed of two interpenetrating hexagonal close-packed (hcp) sublattices, each of which consists of one type of atom displaced with respect to each other along the threefold c-axis by the amount of $u = 3/8 = 0.375$ (in an ideal wurtzite structure) in fractional coordinates. The internal parameter u is defined as the length of the bond parallel to the c-axis (anion–cation bond length or the
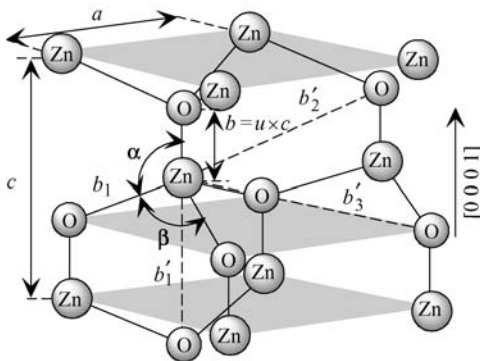
Figure 1.2 Schematic representation of a wurtzitic ZnO structure with lattice constants a in the basal plane and c in the basal direction, u parameter, which is expressed as the bond length or the nearest-neighbor distance b divided by c (0.375 in ideal crystal), α and β (109.47° in ideal crystal) bond angles, and three types of second-nearest-neighbor distances b'_1, b'_2, and b'_3.

nearest-neighbor distance) divided by the *c* lattice parameter. The basal plane lattice parameter (the edge length of the basal plane hexagon) is universally depicted by *a*; the axial lattice parameter (unit cell height), perpendicular to the basal plane, is universally described by *c*. Each sublattice includes four atoms per unit cell, and every atom of one kind (group II atom) is surrounded by four atoms of the other kind (group VI), or vice versa, which are coordinated at the edges of a tetrahedron. The crystallographic vectors of wurtzite are $\vec{a} = a(1/2, \sqrt{3}/2, 0), \vec{b} = a(1/2, -\sqrt{3}/2, 0)$, and $\vec{c} = a(0, 0, c/a)$. In Cartesian coordinates, the basis atoms are (0, 0, 0), (0, 0, *uc*), $a(1/2, \sqrt{3}/6, c/2a)$, and $a(1/2, \sqrt{3}/6, [u+1/2]c/a)$.

In a real ZnO crystal, the wurtzite structure deviates from the ideal arrangement, by changing the *c/a* ratio or the *u* value. The experimentally observed *c/a* ratios are smaller than ideal, as in the case of GaN, where it has been postulated that not being so would lead to zinc blende phase [1]. It should be pointed out that a strong correlation exists between the *c/a* ratio and the *u* parameter in that when the *c/a* ratio decreases, the *u* parameter increases in such a way that those four tetrahedral distances remain nearly constant through a distortion of tetrahedral angles due to long-range polar interactions. These two slightly different bond lengths will be equal if the following relation holds:

$$u = \left(\frac{1}{3}\right)\left(\frac{a^2}{c^2}\right) + \frac{1}{4}. \tag{1.1}$$

The nearest-neighbor bond lengths along the *c*-direction (expressed as *b*) and off *c*-axis (expressed as b_1) can be calculated as

$$b = cu \quad \text{and} \quad b_1 = \sqrt{\frac{1}{3}a^2 + \left(\frac{1}{2} - u\right)^2 c^2}. \tag{1.2}$$

In addition to the nearest neighbors, there are three types of second-nearest neighbors designated as b'_1 (one along the *c*-direction), b'_2 (six of them), and b'_3 (three of them) with the bond lengths [2]

$$b'_1 = c(1-u), \quad b'_2 = \sqrt{a^2 + (uc)^2}, \quad \text{and} \quad b'_3 = \sqrt{\frac{4}{3}a^2 + c^2\left(\frac{1}{2} - u\right)^2}. \tag{1.3}$$

The bond angles, α and β, are given by [2]

$$\alpha = \pi/2 + \arccos\left[\left(\sqrt{1 + 3(c/a)^2(-u + 1/2)^2}\right)^{-1}\right],$$

$$\beta = 2\arcsin\left[\left(\sqrt{4/3 + 4(c/a)^2(-u + 1/2)^2}\right)^{-1}\right]. \tag{1.4}$$

The lattice parameters are commonly measured at room temperature by X-ray diffraction (XRD), which happens to be the most accurate one, using the Bragg law. In ternary compounds, the technique is also used for determining the composition;
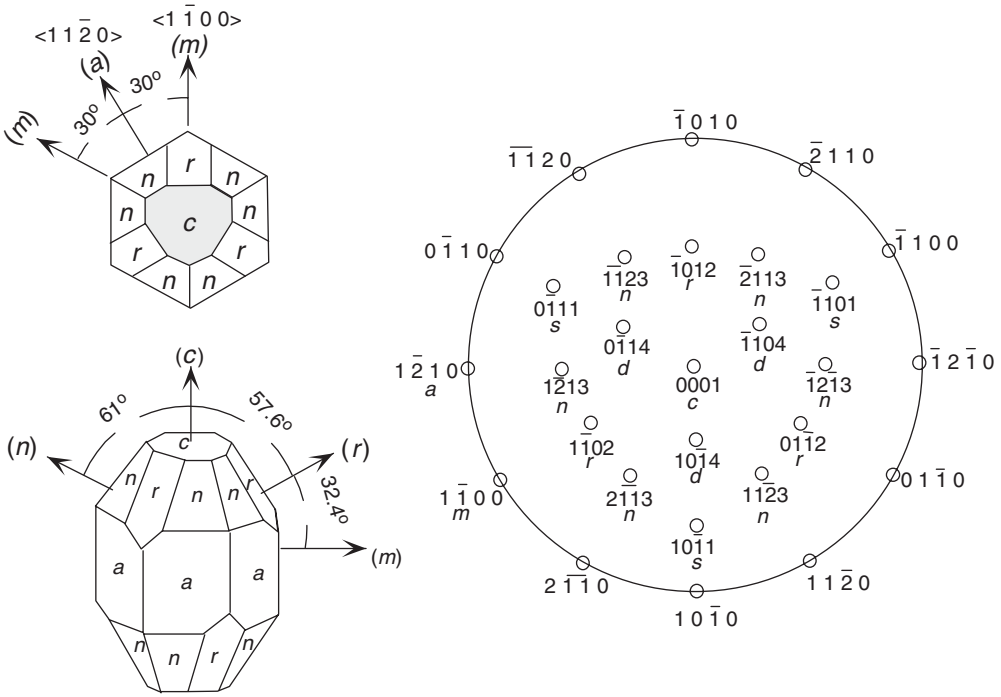
Common crystallographic planes in sapphire		
Plane name	Miller index	d spacing
a	$(11\bar{2}0)$	2.379 Å
m	$(10\bar{1}0)$	1.375 Å
c	(0001)	2.165 Å
r	$(1\bar{1}02)$	1.740 Å
n	$(11\bar{2}3)$	1.147 Å
s	$(10\bar{1}1)$	1.961 Å

Angles between common planes		
$(0001) \wedge (1\bar{1}02)$	$c \wedge r$	57° 35′
$(0001) \wedge (11\bar{2}3)$	$c \wedge n$	61° 11′
$(0001) \wedge (10\bar{1}1)$	$c \wedge s$	72° 23′
$(0001) \wedge (11\bar{2}1)$	$c \wedge$	79° 37′
$(0001) \wedge (11\bar{2}0)$	$c \wedge a$	90° 00′
$(0001) \wedge (10\bar{1}0)$	$c \wedge m$	90° 00′
$(11\bar{2}0) \wedge (10\bar{1}0)$	$c \wedge m$	30° 00′

Figure 1.3 Labeling of planes in hexagonal symmetry (for sapphire).

however, strain and relevant issues must be taken into consideration as the samples are in the form of epitaxial layers on foreign substrates. The accuracy of the X-ray diffraction and less than accurate knowledge of elastic parameters together allow determination of the composition to only within about 1% molar fraction. In addition to composition, the lattice parameter can be affected by free charge, impurities, stress, and temperature [3]. Because the c/a ratio also correlates with the difference of the electronegativities of the two constituents, components with the greatest differences show largest departure from the ideal c/a ratio [4].

The nomenclature for various commonly used planes of hexagonal semiconductors in two- and three-dimensional versions is presented in Figures 1.3 and 1.4. The Wz ZnO lacks an inversion plane perpendicular to the c-axis; thus, surfaces have either a group II element (Zn, Cd, or Mg) polarity (referred to as Zn polarity) with a

(*tuvw*) coordinate system

Figure 1.4 shows hexagonal plane labeling in the (*tuvw*) coordinate system with axes *V*, *t*, *u*, and plane indices including $\bar{1}010$, $\bar{1}120$, $\bar{2}110$, $0\bar{1}10$, $0\bar{1}11s$, $\bar{1}1\bar{2}3n$, $\bar{1}012r$, $\bar{2}113n$, $\bar{1}101s$, $\bar{1}100$, $0\bar{1}14d$, $\bar{1}104d$, $1\bar{2}10a$, $1\bar{2}13n$, $0001c$, $\bar{1}2\bar{1}3n$, $1\bar{2}10$, $1\bar{1}02r$, $0\bar{1}12r$, $1\bar{1}00m$, $2\bar{1}\bar{1}3n$, $10\bar{1}4d$, $11\bar{2}3n$, $01\bar{1}0$, $10\bar{1}1s$, $2\bar{1}\bar{1}0$, $11\bar{2}0$, $10\bar{1}0$.
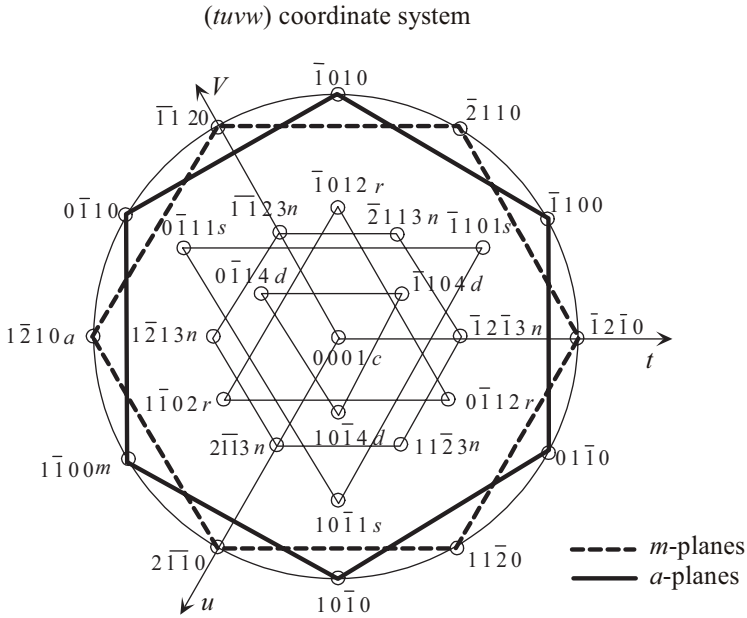
- - - - *m*-planes
——— *a*-planes

Figure 1.4 A magnified view of labeling of planes in hexagonal symmetry in the (*tuvw*) coordinate system with *w* representing the unit vector in the *c*-direction. The lines simply show the symmetry only. If the lines connecting *m*-points among each other and *a*-points among each other were to be interpreted as the projection of those planes on the *c*-plane, the roles would be switched in that the lines connecting the *m*-points would actually represent the *a*-planes and lines connecting the *a*-points would actually represent the *m*-planes, which are normal to the plane of the page.

designation of $(0\,0\,0\,1)$ or $(0\,0\,0\,1)A$ plane or an O polarity with a designation of $(0\,0\,0\,\bar{1})$ or $(0\,0\,0\,\bar{1})B$ plane. The distinction between these two directions is essential due to polarization charge. Three surfaces and directions are of special importance, which are $(0\,0\,0\,1)$, $(1\,1\,\bar{2}\,0)$, and $(1\,\bar{1}\,0\,0)$ planes and the directions associated with them, $\langle 0\,0\,0\,1 \rangle$, $\langle 1\,1\,\bar{2}\,0 \rangle$, and $\langle 1\,\bar{1}\,0\,0 \rangle$, as shown in Figure 1.5. The $(0\,0\,0\,1)$, or the basal plane, is the most commonly used surface for growth. The other two are important in that they represent the primary directions employed in reflection high-energy electron diffraction (RHEED) observations in MBE growth, apart from being perpendicular to one another.

The *zinc blende* ZnO structure is metastable and can be stabilized only by heteroepitaxial growth on cubic substrates, such as ZnS [5], GaAs/ZnS [6], and Pt/Ti/SiO$_2$/Si [7], reflecting topological compatibility to overcome the intrinsic tendency of forming wurtzite phase. In the case of highly mismatched substrates, there is usually a certain amount of zinc blende phase of ZnO separated by crystallographic defects from the wurtzite phase. The symmetry of the zinc blende structure is given by space group $F\bar{4}3m$ in the Hermann–Mauguin notation and T_d^2 in the Schoenflies notation and is composed of two interpenetrating face-centered cubic (fcc) sublattices shifted along the body diagonal by one-quarter of the length of
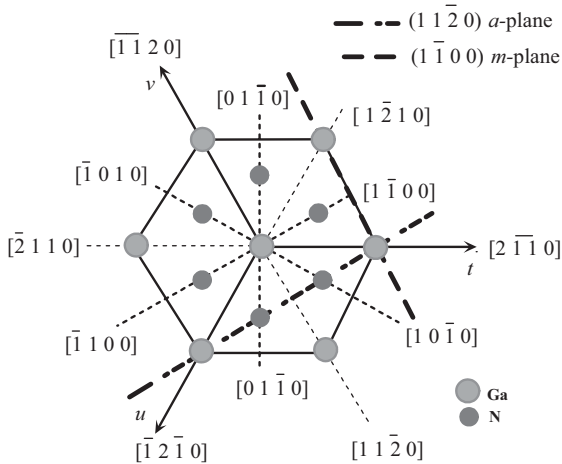
Figure 1.5 Orientations that are commonly used in wurtzite phase, namely, the $(1\,1\,\bar{2}\,0)$ and $(1\,\bar{1}\,0\,0)$ planes and associated directions are shown as projections on the $(0\,0\,0\,1)$ basal plane.

the body diagonal. There are four atoms per unit cell and every atom of one type (group II) is tetrahedrally coordinated with four atoms of other type (group VI), and vice versa.

Because of the tetrahedral coordination of wurtzite and zinc blende structures, the 4 nearest neighbors and 12 next-nearest neighbors have the same bond distance in both structures. Stick-and-ball stacking models for 2H wurtzitic and 3C zinc blende polytypes of ZnO crystals are shown in Figure 1.6. The wurtzite and zinc blende structures differ only in the bond angle of the second-nearest neighbors and, therefore, in the stacking sequence of close-packed diatomic planes. The wurtzite structure consists of triangularly arranged alternating biatomic close-packed $(0\,0\,0\,1)$ planes, for example, Zn and O pairs; thus, the stacking sequence of the $(0\,0\,0\,1)$ plane is AaBbAaBb… in the $\langle 0\,0\,0\,1 \rangle$ direction, meaning a mirror image but no in-plane rotation with the bond angles. In contrast, the zinc blende structure along the $[1\,1\,1]$ direction exhibits a 60° rotation and, therefore, consists of triangularly arranged atoms in the close-packed $(1\,1\,1)$ planes along the $\langle 1\,1\,1 \rangle$ direction that causes a stacking order of AaBbCcAaBbCc…. The point with regard to rotation is very well illustrated in Figure 1.6b. Upper and lower case letters in the stacking sequences stand for the two different kinds of constituents.

Like other II–VI semiconductors, wurtzite ZnO can be transformed to the *rocksalt* (NaCl) structure at relatively modest external hydrostatic pressures. The reason for this is that the reduction of the lattice dimensions causes the interionic Coulomb interaction to favor the ionicity more over the covalent nature. The space group symmetry of the rocksalt type of structure is *Fm3m* in the Hermann–Mauguin notation and O_h^5 in the Schoenflies notation, and the structure is sixfold coordinated. However, the rocksalt structure cannot be stabilized by the epitaxial growth. In ZnO, the pressure-induced phase transition from the wurtzite (B4) to the rocksalt (B1)
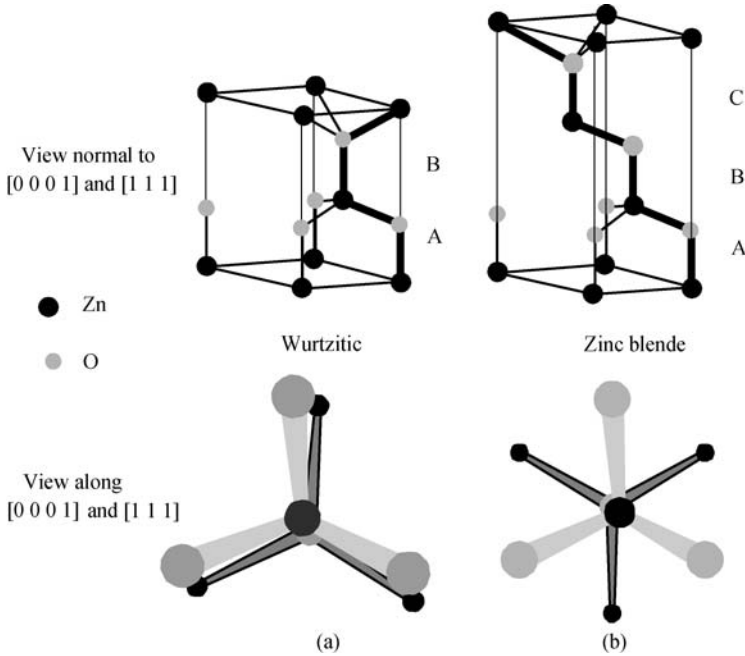
Figure 1.6 Stick-and-ball stacking model of crystals with (a, both top and bottom) 2H wurtzitic and (b, both top and bottom) 3C zinc blende polytypes. The bonds in an *A*-plane ($1 1 \bar{2} 0$) are indicated with heavier lines to accentuate the stacking sequence. The figures on top depict the three-dimensional view. The figures at the bottom indicate the projections on the ($0 0 0 1$) and ($1 1 1$) planes for wurtzitic and cubic phases, respectively. Note the rotation in the case of zinc blende along the $\langle 1 1 1 \rangle$ direction.

phase occurs in the range of 10 GPa associated with a large decrease in volume of about 17% [8]. High-pressure cubic phase has been found to be metastable for long periods of time even at ambient pressure and above 100 °C [8]. Energy-dispersive X-ray diffraction (EDXD) measurements using synchrotron radiation have shown that the hexagonal wurtzite structure of ZnO undergoes a structural phase transformation with a transition pressure $p_T = 10$ GPa and completed at about 15 GPa [9, 10]. The measured lattice-plane spacings as a function of pressure for the B1 phase are shown in Figure 1.7. Accordingly, a large fraction of the B1 phase is retained when the pressure is released indicating the metastable state of the rocksalt phase of ZnO even at zero pressure.

In contrast, using *in situ* X-ray diffraction [11], and later EDXD [12], this transition was reported to be reversible at room temperature. EDXD spectra recorded at pressures ranging from 0.1 MPa to 56 ± 1 GPa at room temperature with increasing and decreasing pressures show a clear wurtzite-to-rocksalt transition starting at 9.1 ± 0.2 GPa with increasing pressure. The two phases coexist over a pressure range of 9.1–9.6 GPa, as shown in Figure 1.8. The structural transition is complete at 9.6 GPa resulting in a 16.7% change in the unit cell volume. Upon decompression, it was observed that ZnO reverts to the wurtzite structure beginning at 1.9 ± 0.2 GPa,
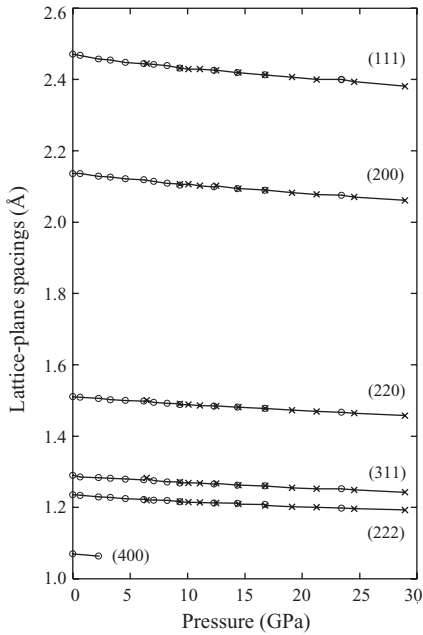
Figure 1.7 Lattice-plane spacing as functions of pressure for the ZnO B1 phase. Crosses denote increasing pressure and circles decreasing pressure. Miller indices *hkl* are indicated for each set of data. (Courtesy of J.M. Recio [10].)

below which only a single wurtzite phase is present. Consequently, the phase hysteresis is substantial. Similar hysteresis was also reported for this transition using X-ray diffraction and Zn Mössbauer spectroscopy [13]. The transition pressure was measured to be 8.7 GPa for increasing pressure whereas it was 2.0 GPa for decreasing pressure.

On the theoretical side, there have been several first-principles studies of compressive parameters of dense ZnO, such as the linear combination of Gaussian-type orbitals (LCGTO), the Hartree–Fock (HF) method [20], the full-potential linear muffin-tin orbital (FP-LMTO) approach to density functional theory (DFT) within the local density approximation (LDA) and generalized gradient approximation (GGA) [14], linear augmented plane wave (LAPW) LDA [13], HF [15], correlated HF perturbed ion (HF-PI) models [10], LCGTO-LDA and GGA methods [10], and the extended ionic model [16]. A critical comparison between experimental and theoretical results can be made for ZnO as the structural and compressive parameters are measured because the dense solid adopts simple structures. These calculations have mostly been limited to the same pressure range as the experiments, and reasonable agreements are realized. Both experimental and theoretical results are summarized in Table 1.1 for comparison.

In addition to the commonly observed and calculated phase transition of ZnO from B4 to B1 at moderate pressures (maximum pressure attained in any experiment on
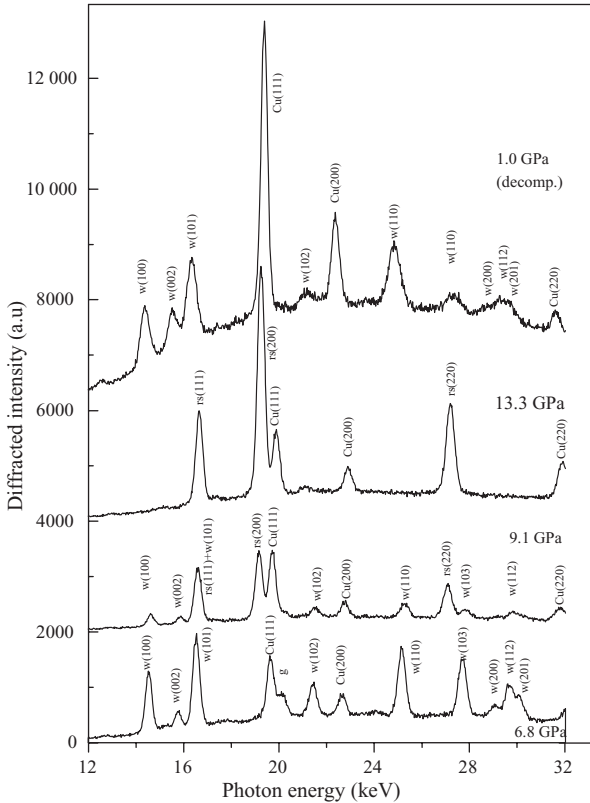
Figure 1.8 Examples of EDXD spectra indicating the coexistence of the wurtzite and rocksalt phases around 9.1 ± 0.2 GPa (increasing pressure) and the emergence of the wurtzite phase $P < 1.9 \pm 0.2$ GPa upon decompression. Spectra are presented in cascade for clarity. Labels w and rs refer to wurtzite and rocksalt, respectively. X-ray diffraction lines from the Cu pressure gauge and the gasket material are labeled as Cu and g, respectively. (Courtesy of S. Desgreniers [12].)

ZnO to date is 56 GPa where the B1 phase remained stable), it has been suggested [17] that at sufficiently high pressures ZnO would undergo a phase transformation from the sixfold-coordinated B1 (cubic NaCl) to the eightfold-coordinated B2 (cubic CsCl) structure, in analogy to the alkali halides and alkaline earth oxides. The transition pressure from B1 phase to B2 phase was predicted at $p_{T2} = 260$ and 256 GPa by employing local density approximation and generalized gradient – corrected local density – approximation, respectively [18], whereas atomistic calculations based on an interatomic pair potential within the shell model approach resulted in a higher value of $p_{T2} = 352$ GPa [19]. However, these theoretical predictions are still awaiting experimental confirmation.

The ground-state total energy of ZnO in wurtzite, zinc blende, and rocksalt structures has been calculated as a function of the unit cell volume using first-principles periodic Hartree–Fock linear combination of atomic orbitals (LCAO)

Table 1.1 Theoretical and experimental compressive parameters of ZnO.

	Experimental results						Theoretical calculations			
	Ref. [8]	Ref. [9]	Ref. [11]	Ref. [12]	Ref. [13]	Ref. [13]	Ref. [14]	Ref. [17]	Ref. [19]	Ref. [20]
Volume, wurtzite (Å^3)	23.829	23.785		23.81	23.796			23.346	23.839	24.570
Volume, rocksalt (Å^3)	19.60	19.60	19.40	19.60	19.484		23.62	19.515	19.041	19.799
Volume change, $\Delta V/V$ (%)	16.7	18.0		17.68	18.13	17.9	19.08	16.41	20.3	19.42
Transition pressure, p_T (GPa)	9.5	10.0	9.0	9.1	8.7	14.5	18.8	9.32	10.45	8.57
							8.0			
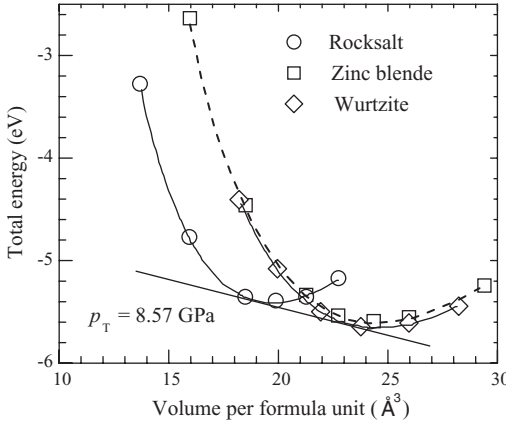
Figure 1.9 Total energy versus volume (both per ZnO formula unit) for the three phases: zinc blende (squares), wurtzite (diamonds), and rocksalt (circles). The zero of energy is the sum of the total energies of an isolated Zn and an isolated O atom. The hexagonal/cubic phase transition occurs at $p_T = 8.57$ GPa. (After Ref. [20].)

theory [20]. The total energy data versus volume for the three phases are shown in Figure 1.9 along with the fits to the empirical functional form of the third-order Murnaghan equation, which is used to calculate the derived structural properties:

$$E(V) = E_0 - \frac{B_0 V_0}{B'-1} + \frac{B_0 V}{B'} \left[\frac{(V_0/V)^{B'}}{B'-1} + 1 \right], \tag{1.5}$$

where E_0, V_0, and B_0 are the total energy, volume per ZnO formula unit, and bulk modulus at zero pressure (P), respectively, and $B' = \mathrm{d}B/\mathrm{d}P$ is assumed to be constant.

In this calculation, although E_0 represents the sum of the total energies of isolated neutral Zn and O atoms, the absolute value of the energy at the minimum of each curve was considered as a rough estimate of the equilibrium cohesive energy of the corresponding ZnO phases. The total energy (or roughly the cohesive energy per bond) in wurtzite variety was calculated to be -5.658 eV for wurtzite, -5.606 eV for zinc blende, and -5.416 eV for rocksalt phases. The density functional theory using two different approximations, namely, the local density and the generalized gradient approximations, in the exchange correlation function was also employed to calculate the total energy and electronic structure of ZnO [18]. In these calculations, cohesive energies were obtained by subtracting the total energy per ZnO formula unit of the solid at its equilibrium lattice constant from the energy of the corresponding isolated atoms. The cohesive energies of ZnO obtained by using the LDA are -9.769, -9.754, and -9.611 eV for wurtzite, zinc blende, and rocksalt structures, respectively. The best agreement with the experimental value of -7.52 eV, which is deduced from experimental Zn heat vaporization, ZnO enthalpy of formation, and O_2 binding energy for the wurtzite phase [21], was achieved using the GGA technique. The GGA

gives -7.692, -7.679, and -7.455 eV cohesive energies for wurtzite, zinc blende, and rocksalt phases, respectively. In these two techniques, although the calculated energy difference ΔE_{W-ZB} between wurtzite and zinc blende lattice is small (about -15 and -13 meV atom^{-1} for LDA and GGA, respectively), whereas it is relatively large, ~ 50 meV atom^{-1}, for Hartree–Fock approximation, the wurtzite form is energetically favorable compared to zinc blende and rocksalt forms.

Because none of the three structures described above possesses inversion symmetry, the crystal exhibits crystallographic polarity, which indicates the direction of the bonds; that is, close-packed (1 1 1) planes in zinc blende and rocksalt (Rochelle salt) structures and corresponding (0 0 0 1) basal planes in the wurtzite structure differ from $(\bar{1}\ \bar{1}\ \bar{1})$ and $(0\ 0\ 0\ \bar{1})$ planes, respectively. The convention is that the [0 0 0 1] axis points from the face of the O plane to the Zn plane and is the positive z-direction. In other words, when the bonds along the c-direction are from cation (Zn) to anion (O), the polarity is referred to as Zn polarity. By the same argument, when the bonds along the c-direction are from anion (O) to cation (Zn), the polarity is referred to as O polarity. Many properties of the material depend also on its polarity, for example, growth, etching, defect generation and plasticity, spontaneous polarization, and piezoelectricity. In wurtzite ZnO, besides the primary polar plane (0 0 0 1) and associated direction $\langle 0\ 0\ 0\ 1 \rangle$, which is the most commonly used surface and direction for growth, many other secondary planes and directions exist in the crystal structure.

1.2
Lattice Parameters

Lattice parameters of ZnO have been investigated over many decades [22–30]. The lattice parameters of a semiconductor usually depend on the following factors: (i) free electron concentration acting via deformation potential of a conduction band minimum occupied by these electrons, (ii) concentration of foreign atoms and defects and their difference of ionic radii with respect to the substituted matrix ion, (iii) external strains (e.g., those induced by substrate), and (iv) temperature. The lattice parameters of any crystalline material are commonly and most accurately measured by high-resolution X-ray diffraction (HRXRD) using the Bond method [31] for a set of symmetrical and asymmetrical reflections. Table 1.2 tabulates measured and calculated lattice parameters, c/a ratio, and u parameter reported by several groups for ZnO crystallized in wurtzite, zinc blende, and rocksalt structures for comparison.

The room-temperature lattice constants determined by various experimental measurements and theoretical calculations for the wurtzite ZnO are in good agreement with each other. The lattice constants mostly range from 3.2475 to 3.2501 Å for the a-parameter and from 5.2042 to 5.2075 Å for the c-parameter. The data produced in earlier investigations, reviewed by Reeber [30], are also consistent with the values given in Table 1.2. The c/a ratio and u parameter vary in a slightly wider range, from 1.593 to 1.6035 and 0.383 to 0.3856, respectively. The deviation from that of the ideal wurtzite crystal is probably due to lattice stability and ionicity. It has been reported that free charge is the dominant factor responsible for expanding

Table 1.2 Measured and calculated lattice constants and the *u* parameter of ZnO.

Wurtzite				
a (Å)	*c* (Å)	*c/a*	*u*	Reference
		1.633	0.375	Ideal
3.2496	5.2042	1.6018	0.3819	a
3.2501	5.2071	1.6021	0.3817	b
3.286	5.241	1.595	0.383	c
3.2498	5.2066	1.6021		d
3.2475	5.2075	1.6035		e
3.2497	5.206	1.602		f
		1.593	0.3856	g
		1.600	0.383	h

Zinc blende (sphalerite actually)
4.619[c], 4.60[g], 4.463[i], 4.37[i], 4.47[i]

Rocksalt (Rochelle salt)
4.271[a], 4.283[d], 4.294[e], 4.30[g], 4.280[j], 4.275[k], 4.058[k], 4.316[k], 4.207[k], 4.225[l]

[a]Measured by using XRD [13].
[b]Measured by using XRD [4].
[c]Calculated by using *ab initio* periodic LCAO method, based mainly on the Hartree–Fock
Hamiltonian, with an all-electron Gaussian-type basis set [32].
[d]Measured by using EDXD [12].
[e]Measured by using XRD [9].
[f]Measured by using XRD [30].
[g]Calculated by using first-principles periodic Hartree–Fock LCOAO program [20].
[h]Calculated by using *ab initio* quantum mechanical level through the Berry phase scheme applied to
  delocalized crystalline orbitals and through the definition of well-localized Wannier functions [33].
[i]Measured by using RHEED, XRD, and TEM [6].
[j]Measured by using XRD [8].
[k]Measured by using EDXD and calculated by using Coulomb Hartree–Fock perturbed ion, GGA, and
  LDA methods [10].
[l]Calculated by using first-principles periodic Hartree–Fock [15].

the lattice proportional to the deformation potential of the conduction band minimum and inversely proportional to the carrier density and bulk modulus. The point defects such as zinc antisites, oxygen vacancies, and extended defects, such as threading dislocations, also increase the lattice constant, albeit to a lesser extent in the heteroepitaxial layers.

For the zinc blende polytype of ZnO, the calculated lattice constants based on modern *ab initio* technique are predicted to be 4.60 and 4.619 Å. Zinc blende ZnO films have been grown by using ZnS buffer layers [6]. The lattice constant was estimated to be 4.463, 4.37, and 4.47 Å by using the spacing of RHEED pattern, albeit spotty, comparing the XRD peak position, and examining the transmission electron microscopy (TEM) images, respectively. These values are far from wurtzite phase indicating the formation of zinc blende ZnO. The lattice constant measured with the RHEED technique is in very good agreement with the theoretical predictions.

High-pressure phase transition from the wurtzite to the rocksalt structure decreases the lattice constant down to the range of 4.271–4.294 Å. The experimental values obtained by X-ray diffraction are in close agreement. The predicted lattice parameters of 4.058–4.316 Å, using various calculation techniques such as the HF-PI, GGA, and HF, are about 5% smaller or larger than the experimental values. The dispersion in the calculated values is larger than the measured ones.

The ideal relationship between the c/a axial ratio and the u oxygen positional parameter is preserved as the wurtzite ZnO lattice becomes denser while approaching the structural transition pressure [12]. The change in the c/a axial ratio was measured up to ∼10 GPa, and a pressure coefficient of $d(c/a)/dP = -0.0005$ 0.0001 GPa^{-1} was obtained from a linear fit (giving $c/a = 1.6021$ at atmospheric pressure) to the experimental data. Even though the variation with pressure seems within the experimental error, this pressure coefficient is in agreement with the previously published experimental (-0.0007 GPa^{-1}) [13] and predicted (-0.0005 GPa^{-1}) [20] values. The effect of pressure-induced change in the axial ratio on the u parameter against a possible breakdown of the ideal relationship between the axial ratio and u was isolated by recording pressure dependence variation of X-ray diffraction intensity.

1.3
Electronic Band Structure

The band structure of a given semiconductor is pivotal in determining its potential utility. Consequently, an accurate knowledge of the band structure is critical if the semiconductor in question is to be incorporated in the family of materials considered for device applications. Several theoretical approaches with varying degrees of complexity have been employed to calculate the band structure of ZnO for its wurtzite, zinc blende, and rocksalt polytypes. Besides, a number of experimental data have been published regarding the band structure of the electronic states of wurtzite ZnO. X-ray or UV reflection/absorption or emission techniques have conventionally been used to measure the electronic core levels in solids. These methods basically measure the energy difference by inducing transitions between electronic levels (e.g., transitions from the upper valence band states to the upper conduction band states and from the lower valence band states) or by exciting collective modes (e.g., the upper core states to the lower edge of the conduction band and to excitations of plasmons). Another important method for the investigation of the energy region is based on the photoelectric effect extended to the X-ray region, namely, photoelectron spectroscopy (PES). The peaks in emission spectrum correspond to electron emission from a core level without inelastic scattering, which is usually accompanied by a far less intense tail region in the spectrum. Additionally, angle-resolved photoelectron spectroscopy (ARPES) technique together with synchrotron radiation excitation have been recognized as a powerful tool that enables the determination of experimental bulk and surface electronic band structures under the assumptions of k-conservation and single

nearly free-electron-like final band [34]. After the first theoretical work on band structure calculation of ZnO proposed by Rössler using Green's function (Korringa–Kohn–Rostoker (KKR) method) [35] in 1969, several experimental works [36–39] have been performed on the wurtzite ZnO, which proved Rössler's predicted bulk electronic structure to be far from satisfactory. The first experimental data related to the energy levels of core electrons in ZnO were obtained by using X-ray induced photoemission spectroscopy [36]. Consequently, the location of the Zn 3d level in ZnO was unambiguously determined and the discrepancy between the measured values and the theoretically determined energy values was found to be dependent on angular momentum. UV photoemission measurements on hexagonal ZnO cleaved in vacuum showed the Zn 3d core level at about 7.5 eV below the valence band maximum [37, 38], which is 3 eV lower than the value predicted by Rössler's band calculation. This assignment is in good agreement with X-ray photoemission measurements that produced 8.5 eV [40] and 8.81 eV [39]. In the ensuing years, local density approximation and tight-binding methods were carried out [41–44] by considering the Zn 3d states as core levels to simplify calculations. Satisfactory agreement with qualitative valence band dispersions was achieved with this assumption. However, quantitative disagreements remained and the location of the Zn 3d states could not be predicted. With the advent of new computer capabilities, theoretical works began to include the effect of Zn 3d level in the calculations and thus considering them as valence band states [45–48]. These methods enable an estimation of the position of the Zn 3d states and also take into account their non-negligible influence on the s- and p-derived valence bands.

Angle-resolved photoelectron spectroscopy has been employed to study the electronic structure of the ZnO (0 0 0 1) [49]. Recording both normal and off-normal emission spectra gives valuable information about bulk and surface states as well as the Zn 3d states. Figure 1.10 shows some of the normal emission spectra recorded at photon energies ranging from 20 to 50 eV and the information extracted from these data for bulk band structure. In these measurements, the binding energies were referred to the Fermi level and the intensities were normalized to the photon flux. Among all the spectra displayed, seven features were observed, labeled from A to G. The dispersions of the four valence bands observed in the (0 0 0 1) direction were compared with theory based on LDA calculations, which consider the Zn 3d electrons as part of the valence band [45] and good agreement was realized. It should also be noted that the Zn 3d states were observed to separate into two groups of four and six bands, which show dispersion with k, which is in agreement with theoretical results, but the locations of these states (about 10.5 eV below Fermi level) were not accurately predicted.

The polar (0 0 0 1)-Zn and (0 0 0 $\bar{1}$)-O surfaces and the nonpolar (1 0 $\bar{1}$ 0) surface (*m*-plane) have also been the object of experimental and theoretical investigations. Of these surfaces, the nonpolar (1 0 $\bar{1}$ 0) surface is of particular interest from the viewpoint of surface chemistry, because the surface is terminated with the same number of O and Zn atoms. The low-energy electron diffraction (LEED) studies have revealed that the surface undergoes relaxation, which is characterized by downward shift (spatially) of both surface Zn and O atoms, with a greater shift for the Zn atom
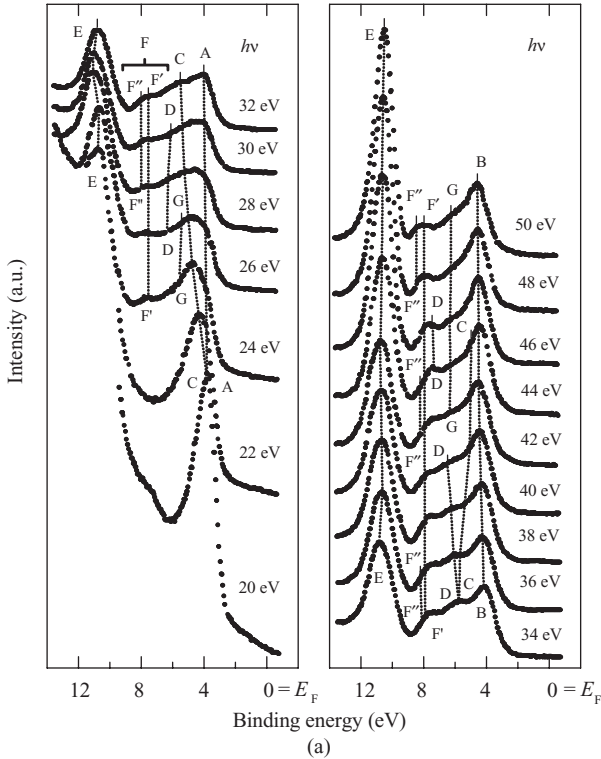
Figure 1.10 (a) Normal emission spectra for photon energies ranging between 20 and 50 eV. The spectra were normalized with respect to the photon flux. (b) Bulk band structure of ZnO, ΓA corresponding to $0.6\,\text{Å}^{-1}$. (After Ref. [49].) The dashed lines are the LDA calculation results reproduced from Schröer *et al.* [45].

than the O atom, resulting in the Zn−O bond rotation by 6.2° [50] or 11.5° [51] with respect to the ideal surface plane. Such a surface relaxation should influence the energetic position as well as the dispersion width of the surface dangling bond bands of the occupied O 2p and unoccupied Zn 4s states. Besides, several theoretical studies have indicated that, upon relaxation, the O 2p dangling bond state is stabilized while the Zn 4s dangling bond state shifts up in energy [43, 47, 52]. The theoretically determined position of these dangling bond bands, especially the occupied O 2p dangling bond band, relative to the bulk bands projected onto the (1 0 $\bar{1}$ 0) surface varies depending on the method employed in the calculations.

Surface states have been revealed in ARPES studies of both polar and nonpolar ZnO surfaces. In one particular study [53], two surface-induced features at the Γ, M, and X points of the surface Brillouin zone (BZ) have been identified and assigned to the O 2p-derived dangling bond state and the Zn–O backbond state. Similarly, the